RESEARCH ARTICLE

Key Points:
- We present a new 3-D shear-wave velocity model for the crust and uppermost mantle beneath the Alaskan Cordillera
- We observe a low-velocity mantle wedge that extends further east than located slab seismicity
- Our results are consistent with numerous lithospheric structures seen in previous geophysical studies

Lithospheric Structure Across the Alaskan Cordillera From the Joint Inversion of Surface Waves and Receiver Functions

Kevin M. Ward[1,2] (ID) and Fan-Chi Lin[1] (ID)

[1]Department of Geology and Geophysics, University of Utah, Salt Lake City, UT, USA, [2]Now at Department of Geology and Geological Engineering, South Dakota School of Mines & Technology, Rapid City, SD, USA

Abstract The final deployment stage of the USArray Transportable Array is nearly complete with several years of high-quality broadband seismic data across the Northern American Cordillera already publicly available. This section of the Cordillera represents a rich history of tectonic deformation and accretion events as well numerous active tectonic processes. Many of these active tectonic processes such as uplift mechanisms or magmatic systems have been interpreted from structures imaged in regional or limited 2-D studies. To investigate the fully 3-D nature of the crust and uppermost mantle ($<$70 km), we present the results of a joint receiver function, surface wave inversion for the shear wave velocity structure across the Alaskan Cordillera. Integration of our new isotropic velocity model with existing data sets, including seismicity, gravity anomalies, and other seismic imagining methods, indicates that our velocity model is consistent with previous studies while providing unprecedented additional detail. A prominent feature in our model is a low-velocity mantle wedge. We suggest this low-velocity mantle wedge results from subducting slab lithosphere. The tectonic significance of this interpretation is that the velocity anomaly extends further to the east than slab seismicity does, suggesting that the downgoing slab extends further to the east, albeit aseismicly. This interpretation provides a simple explanation for the location of the active Wrangell volcanoes. We expect that our velocity model will be integrated with other mantle tomography models to further refine our understanding of this complex tectonic setting.

1. Introduction

The formation of the Northern American Cordillera in Alaska and westernmost Canada records a long history of accretion and deformation with the earliest known deformation occurring in the Paleoproterozoic (Turner et al., 2009). Continuing deformation is evidenced by the ongoing collision of the Yakutat Terrane along the southern active subduction zone margin (Plafker, 1987). In general, the Alaskan Cordillera can be subdivided into three regions with unique deformation histories (Moore & Box, 2016). The northern region is characterized by Early Cretaceous oceanic-continental collision and subsequent mid-Cretaceous extension. The central or interior region is mostly characterized Permian extensional and collisional deformation. The southern and most active region is characterized by Mesozoic and younger terrane accretion events (Trop & Ridgway, 2007) and includes the actively colliding Yakutat Terrane. In addition to a long history of Cordilleran style of deformation, the southern active margin is home to a wide range of plate kinematic boundaries including: oceanic-oceanic convergence, oceanic-continental convergence, and continental-continental transpression (Plafker & Berg, 1994). Furthermore, the geometry of the long-lived (Rioux et al., 2010) subducting slab appears to vary greatly over the southern margin from a normal dip in the west along the Aleutians to a shallow/flat slab geometry associated with the Yakutat Terrane in the east (Eberhart-Phillips et al., 2006). Thus, this section of the North American Cordillera provides one of the most unique (and relatively understudied) settings to study the effects of both long-lived and active Cordilleran style tectonics (Figure 1).

Until recently, geophysical studies of the Northern American Cordillera have been somewhat limited in scope to smaller regional studies. This is mainly a result of the remote location, rugged topography, and harsh environmental conditions that make working in this area of the world exceptionally difficult. With the final stage of the USArray Transportable Array (TA) sweeping across the Alaskan Cordillera (IRIS Transportable Array, 2003), high-quality, near real-time publicly available broadband seismic data are now available on a scale previously unavailable for this region. In this study, we combine ambient noise tomography and receiver functions to
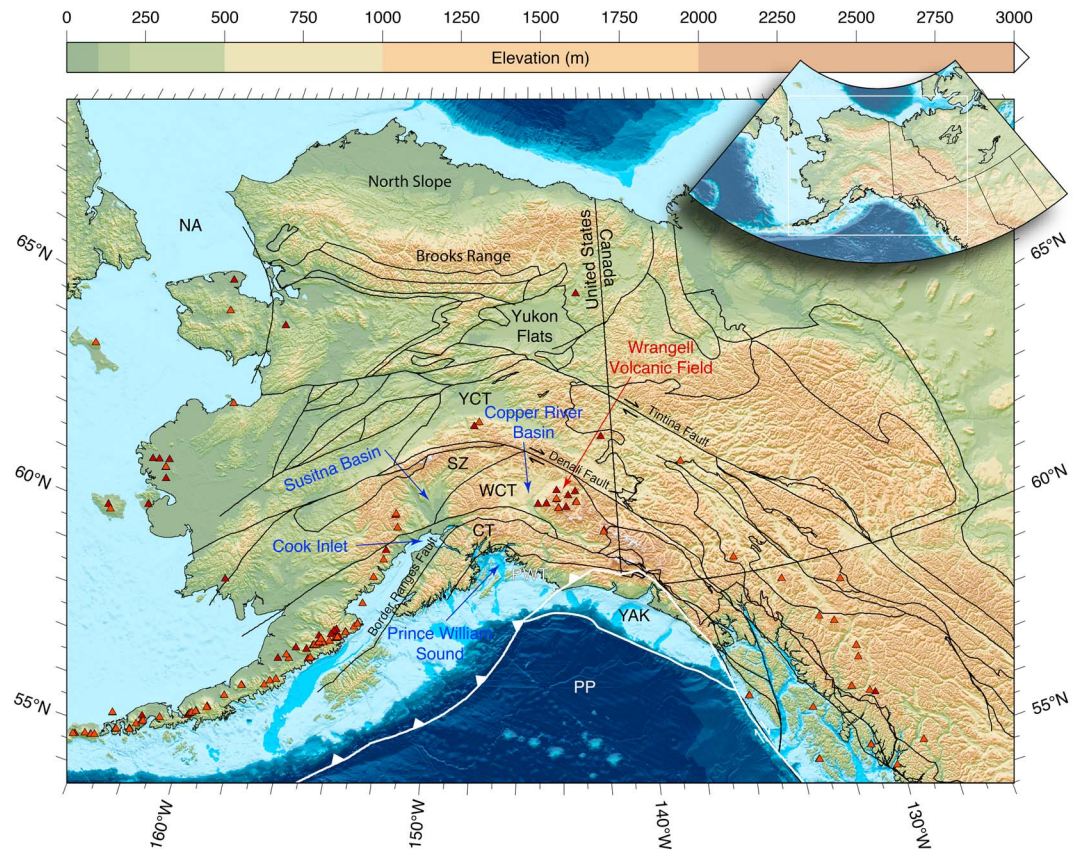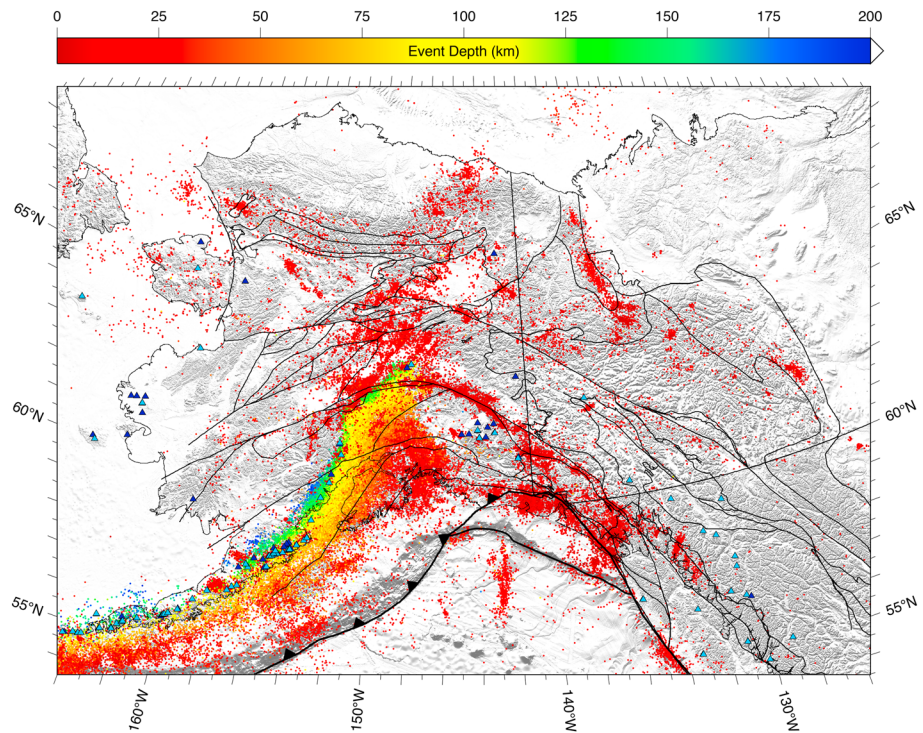
Figure 1. Topography and tectonic setting map across our study area. Holocene volcanic activities from the Smithsonian Institution Global Volcanism Program are shown as red triangles, and the dark red triangles show older (<2 Ma) volcanic activity from the Alaska Volcano Observatory. The black lines show major terrane boundaries (Colpron et al., 2007). YCT, Yukon Composite Terrane; SZ, Alaska Range Suture zone; WCT, Wrangellia Composite Terrane; CT, Chugach Terrane; PWT, Prince William Terrane; YAK, Yakutat Terrane; NA, North American Plate; PP, Pacific Plate.

generate a 3-D shear wave velocity model for the crust and uppermost mantle (~60- to 70-km depth) using the newly available TA broadband seismic data.

Our 3-D shear wave velocity model has a twofold purpose. First, we compare our new velocity model with existing 1-D and 2-D results from smaller regional scale studies to better refine the tectonic interpretations of both existing studies and our own velocity model (e.g., the location of the crust-mantle transition and proposed uplift mechanisms). Furthermore, our new Cordilleran-scale velocity model allows us to integrate our results with larger-scale data sets, such as the distribution of seismicity (Figure 2) and Bouguer gravity anomalies (Figure 3). These comparisons not only aid us in refining our tectonic interpretations (e.g., eastward extent of subducting lithosphere) but also help in establishing the robustness of our velocity model results. Second, we intend to make our velocity model publicly available for use in future studies as a data product. With the final USArray TA configuration now deployed and expected to collect several years of continuous data, we hope our velocity model can be used to help in the generation of deeper mantle imaging studies or with comparisons from other crustal and uppermost mantle geophysical models.

2. Data and Methods

In general, we apply the same data processing and methods used by Ward et al. (2014) to generate a 3-D lithospheric scale (~70 km) shear wave velocity model for the Alaskan Cordillera. Vertical component broadband seismic data from the recently deployed TA are used to generate a series of 2-D Rayleigh wave phase velocity maps. Rayleigh wave dispersion measurements made from a previous ambient noise tomography study in the area (Ward, 2015) are used to augment the results in this study. Radial receiver functions are

Figure 2. Seismicity location map across our study area. Events from 1 January 1990 through 30 June 2017 with any kind of magnitude over 1.0 from the Alaska Earthquake Center. Holocene volcanic activities from the Smithsonian Institution Global Volcanism Program are shown as blue triangles, and the dark blue triangles show older (<2 Ma) volcanic activity from the Alaska Volcano Observatory. The black lines show major terrane boundaries (Colpron et al., 2007).

calculated from both the newly available Cordilleran scale TA deployment and smaller regional scale temporary broadband deployments. Individual 1-D joint inversions of surface wave dispersion and radial receiver functions are systematically assembled into our final 3-D shear wave velocity model. Details of the specific processing and data used in this study are presented in the following subsections.

2.1. Data

The primary data set used in the generation of our 3-D shear wave velocity model presented in this study is sourced from a virtual network of permanent and temporary broadband seismic stations (Figure 4). That virtual network includes data from the TA (IRIS Transportable Array, 2003), the Alaska Regional Network (AK; Alaska Earthquake Center, Univ. of Alaska Fairbanks, 1987), the National Tsunami Warning Center Alaska Seismic Network (AT; NOAA National Oceanic and Atmospheric Administration (USA), 1967), the Canadian National Seismograph Network (CN; Geological Survey of Canada, 1989), the United States National Seismic Network (US; Albuquerque Seismological Laboratory (ASL)/USGS, 1990), the Broadband Experiment Across the Alaska Range (XE; Christensen et al., 1999), the Observational and Theoretical Constraints on the Structure and Rotation of the Inner Core (XR; Song & Christensen, 2004), and the Multidisciplinary Observations Of Subduction (YV; Abers & Christensen, 2006). In total, 204 stations recording continuous data from June 2014 through May 2017 are used in our Rayleigh wave analysis (Figure 4, gold and green circles). However, data from an earlier epoch are effectively included with the addition of Rayleigh wave dispersion measurements from a previous study (Ward, 2015). Our receiver function analysis includes data from 267 stations (Figure 4, blue and green circles) recorded discontinuously from May 1999 through May 2017.

2.2. Ambient Noise Tomography

Ambient noise tomography is an effective, and now standard, technique for extracting meaningful signals from diffuse (practically) seismic wavefields (Shapiro et al., 2005). In this study, we follow the standard data preprocessing outlined by Bensen et al. (2007), Lin et al. (2008), and thoroughly described by Ward (2015;
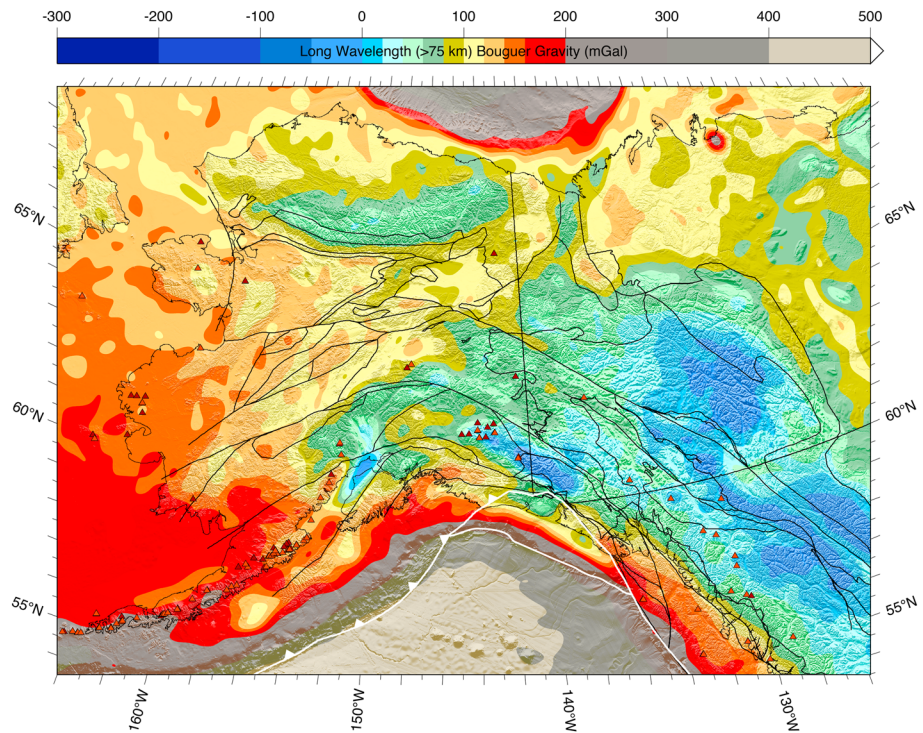
Figure 3. Long wavelength (>75 km) Bouguer gravity anomaly map for our study area (Bonvalot et al., 2012). Holocene volcanic activities from the Smithsonian Institution Global Volcanism Program are shown as red triangles, and the dark red triangles show older (<2 Ma) volcanic activity from the Alaska Volcano Observatory. The black lines show major terrane boundaries (Colpron et al., 2007).

supporting information) to extract interstation Rayleigh wave phase dispersion measurements from 8- to 40-s period (Figure S1 in the supporting information). Interstation dispersion measurements from Ward (2015) are combined with new measurements from this study and then are inverted for 2-D phase velocity maps as a function of period (Figures 5 and S2). For this inversion, we use the straight-ray approach (Figure S3) of Barmin et al. (2001) with a model grid geometry of 0.25° by 0.25°. A measure of lateral resolution after performing the 2-D phase velocity inversion is also available for each period (Figure S4). However, we limit the discussion and interpretation of our model to areas within 100 km of stations where 1-D joint inversion results are available (Figure 4, white contour).

2.3. Receiver Functions

Converted wave imaging (e.g., receiver functions) is particularly useful at imaging the layered structure of the Earth (Langston, 1979). In this study, we use the iterative time domain deconvolution method of Ligorria and Ammon (1999) to generate radial receiver functions from teleseismic (30° to 90°) events with a magnitude (M_w) greater than or equal to 6.0. The event windowed vertical and radial waveforms are bandpassed filtered between 20 s and 4 Hz with the resulting receiver functions having a maximum frequency content of ~1.2 Hz (Gaussian "a" value of 2.5). We apply an automated quality control filter to the resulting ~150,000 receiver functions to ensure that the near-zero time-lag pulse is positive and larger in absolute amplitude than any other subsequent arrivals. The culled receiver functions are paired with Rayleigh wave phase velocity measurements in the subsequent joint 1-D inversion.

2.4. 1-D Joint Shear-Wave Velocity Inversion

Our 1-D joint shear wave velocity inversion follows the linearized damped least squares approach developed by Julià et al. (2000). Each surviving receiver function from the initial quality control filter is paired with a 1-D dispersion curve corresponding to the specific station location where the receiver function was generated and jointly inverted for a 1-D shear wave velocity model (Herrmann & Ammon, 2004). Thus, each station has a distribution of 1-D shear wave velocity models (Figure 6b)
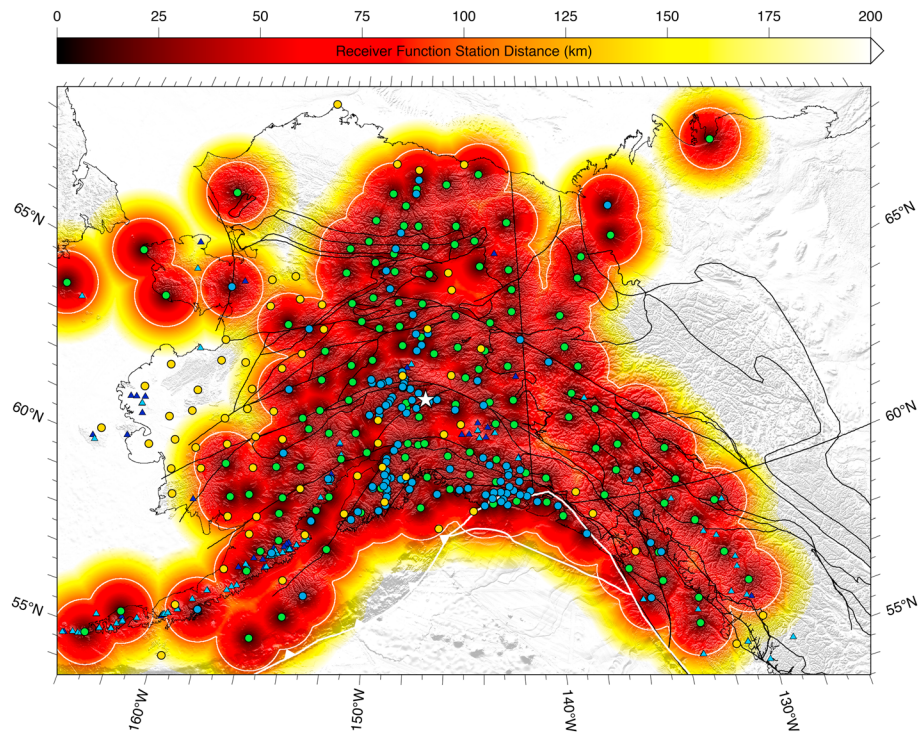
Figure 4. Broadband station location map across our study area. The colored circles indicate stations that were used in both our receiver function and surface waves analysis (green circles), stations that only contributed to our receiver function analysis (blue circles), and stations that only contributed to our surface wave analysis (gold circles). Distance from stations included in our receiver function analysis are plotted in the background and used as a qualitative proxy for model robustness (white 100-km distance contour). Holocene volcanic activities from the Smithsonian Institution Global Volcanism Program are shown as blue triangles, and the dark blue triangles show older (<2 Ma) volcanic activity from the Alaska Volcano Observatory. The black lines show major terrane boundaries (Colpron et al., 2007). The white star shows location of station example plotted in Figure 6.

equal to the number of receiver functions generated at each station (Figure 6d). Although, on average, each station has more than 130 individual 1-D shear wave velocity models, we require each station to have at least 10 receiver functions in the final distribution. This helps to reduce azimuthal bias from stations that were only operating for a short while at the time of this study with fewer receiver functions available for use.

For each 1-D shear wave velocity inversion, we use a homogeneous constant velocity staring model parameterized with 1-km thick layers in the first 80 km, followed by 10 layers that dilate in thickens from 5 km to 50 km, over a half space. Thus, no Moho is imposed in the starting model and no Moho as a parameter is solved for during the inversion. Where the Moho signal (or any discontinuity) is stronger in the receiver function data, the resulting smoothed velocity model has a larger vertical velocity gradient but no distinct velocity step. The large-scale features we seek to image in this study are sufficiently resolved by using a homogeneous constant velocity staring model as we employ an iterative approach. During the inversion, the receiver function misfit is weighted approximately 4 times that of the surface wave dispersion misfit. This helps to extract the character of the structure from the receiver functions (which can be harder to fit than the dispersion data) while still satisfying the dispersion data. The inversion is allowed to iterate up to 30 times but is terminated when the misfit to the data is not improving by 1% over the previous iterations misfit. In practice, this 1% threshold is somewhat arbitrary, as a 5% threshold would terminate the inversion at the same iteration about 90% of the time (within two iterations 100% of the time). The final 1-D shear wave model for each station is the mean of the resulting distribution (Figure 6b, blue line). The resulting 267 1-D shear wave models serve as the starting model for a surface wave only, 3-D shear wave velocity inversion.
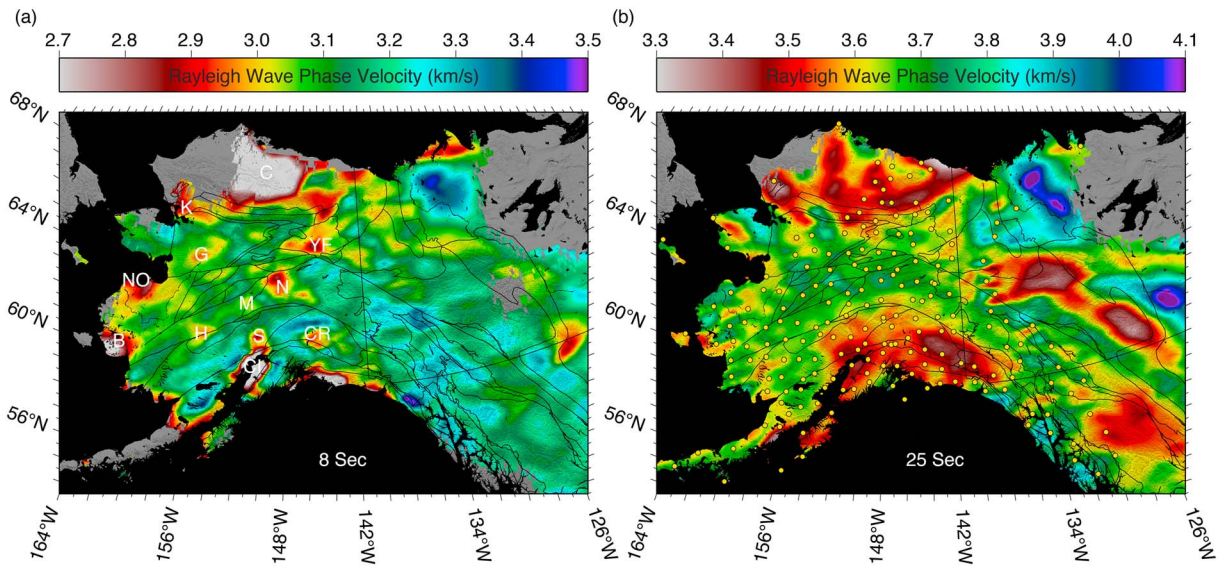
Figure 5. Rayleigh wave phase velocity results for 8- and 25-s periods. (a) The 8-s period map highlights basins across our study area (e.g., low phase velocities). C, Colville Basin; K, Kotzebue Basin; YF, Yukon Flats Basin; G, Galena Basin; NO, Norton Basin; N, Nenana Basin; M, Minchumina Basin; B, Bethel Basin; H, Holitna Basin; S, Susitna Basin; CR, Copper River Basin; and CI, Cool Inlet Basin (Kirschner, 1988). (b) The 25-s period map highlights the large crustal thickness variations across our study area (e.g., sharp changes in phase velocities across terrane boundaries). The gold circles show the locations of stations used in our surface wave analysis. Note that additional stations located off this map were included in our surface wave analysis. However, since they were not used in our receiver function analysis and are not included in our final velocity model, we have not plotted them here. The black lines show major terrane boundaries (Colpron et al., 2007). Additional Rayleigh wave phase velocity results are included in Figure S2, along with the ray geometry for each period (Figure S3), and the resolution for each period (Figure S4).

2.5. 3-D Shear-Wave Velocity Assembly

To incorporate the 1-D structural constraints provided by the receiver functions at each station with the 3-D velocity information from the surface wave dispersion data across the virtual array, we interpolate the irregularly spaced 1-D shear wave velocity profiles into a regularly gridded 3-D model using the natural neighbor algorithm (Sibson, 1980, 1981). The resulting shear wave velocity volume has the same grid geometry (0.25° by 0.25°) as the 2-D phase velocity maps and serves as the starting model for a surface wave only inversion (Herrmann & Ammon, 2004). The inversion is allowed to iterate up to 10 times but is terminated when the misfit to the data is not improving by 1% over the previous iterations misfit. At locations with receiver function constraints, the final shear wave velocity model does not change much but is still within one standard deviation (Figure 6b, red line) of the joint 1-D model mean. This is because in the initial 1-D joint inversion, the receiver functions are weighted approximately 4 times that of the surface wave dispersion and also because the final 1-D joint inversion results are a mean of the model distribution rather than any single inversion solution. This approach ensures that the final 3-D shear wave velocity model satisfies the dispersion data (Figure S5) while simultaneously incorporating structural constraints provided by the receiver functions.

In our final 3-D shear wave velocity model, lateral resolution is strongly controlled by the station distribution. Grid points in the final 3-D model that are closer to grid-points with a 1-D joint inversion result are better-constrained and less nonunique. Thus, we use the interstation distance as a proxy (Figure 4) for lateral model resolution and limit our discussion of results to areas less than 100 km from a grid point with a 1-D joint inversion result, although the average interstation distance is less than 50 km (<2 grid points). Depth sensitivity is also variable across our final 3-D shear wave velocity model but is largely controlled by the sensitivity of the longest period surface wave used in this study (40-s period). Although the peak sensitivity at 40-s period varies across our final model space between 60- and 70-km depth, we limit our discussion of results to depths of less than 70 km. We further evaluate the robustness of our final 3-D velocity model by comparing our results with other geophysical studies and geology structures by highlighting areas of agreement and focusing on newly resolvable features.
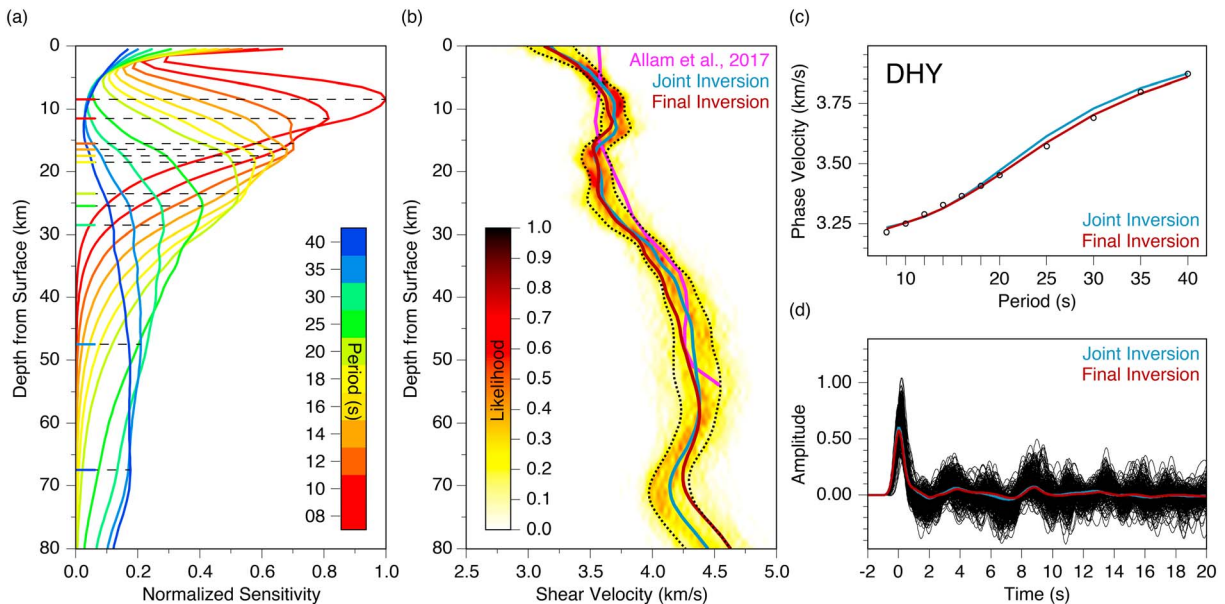
Figure 6. .One-dimensional Joint, surface wave only inversion results, and sensitivity kernels for an example station (DHY) located in the Wrangellia Composite Terrane south of the Denali fault (location shown as white star in Figure 4). (a) Normalized Rayleigh wave phase velocity sensitivity kernels for each of the 11 periods used in this study for the final shear wave velocity model at this location. (b) Probability density plot for all of the joint receiver function and surface wave 1-D shear wave inversion results at this location with the mean of the models shown as the blue line that serves as the starting model for the final surface wave only inversion (see main text for difference). Plus/minus one standard deviation of the shear wave model ensemble distribution is shown as dashed black lines with the final surface wave only shear wave velocity inversion results shown with a red line. Note that the final surface wave only shear wave velocity inversion results fit the dispersion data slighter better while still falling within one standard deviation of the shear wave model ensemble distribution. For comparison, a 1-D Vs profile from a recent body wave tomography study is also shown as a purple line for this location (Allam et al., 2017). (c) Rayleigh wave phase velocity dispersion data from this study shown as open circles for this location. Predicted Rayleigh wave phase velocity dispersion curves for the joint receiver function and surface wave 1-D shear wave model shown as a blue curve with the final surface wave only 1-D shear wave model shown as a red curve. (d) Every receiver function used at this location (268 RFs) is shown as black waveforms. The predicted receiver function from the mean of the joint receiver function and surface wave 1-D shear wave inversions results shown as a blue line and the predicted receiver function from the final surface wave only 1-D shear wave model shown as a red line (modeled using a 0.06-s/km ray parameter/horizontal slowness).

3. Results

The complete shear wave velocity model will be available from IRIS Data Services Products: Earth Model Collaboration (https://ds.iris.edu/ds/products/emc/). At this interface, any map slice or cross section from the model can be plotted using the "visualization tools" feature or the model can be extracted in digital form for use in other applications (Hutko et al., 2017). It is our intention that the complete model be made available (not just the select slices shown here) for integration into other studies where possible. For this reason, our final 3-D shear wave velocity model is presented as a limited series of map slices (Figure 7) and cross sections (Figure 8) from which we highlight large-scale features of tectonic interest. Additional horizontal depth slices are included in the supporting information (Figure S6).

3.1. Sedimentary Basins

Where available, sedimentary basins provide one of the best qualitative measures of a velocity models robustness because basins are typically well mapped and associated with strong slow velocity anomalies. Thick sequences of Cenozoic (Kirschner, 1988) and Cretaceous (Moore & Box, 2016) sediments are clearly identified in the short-period phase velocity maps (Figure 5a) with corresponding velocity anomalies observable in the shallow shear wave velocity results (Figure 7a). This suggests that our joint inversion scheme is accurately translating the surface wave dispersion and receiver function data into our final shear wave velocity model, including subtler features, which might not have as strong of a velocity perturbation as sedimentary basins. As the focus of this study is the large-scale crustal and uppermost mantle structures, we limit our discussion of sedimentary basins to a qualitative measure of model robustness. Future studies that incorporate Rayleigh wave ellipticity (i.e., H/V ratios) will be better positioned to quantify shallow crustal features.
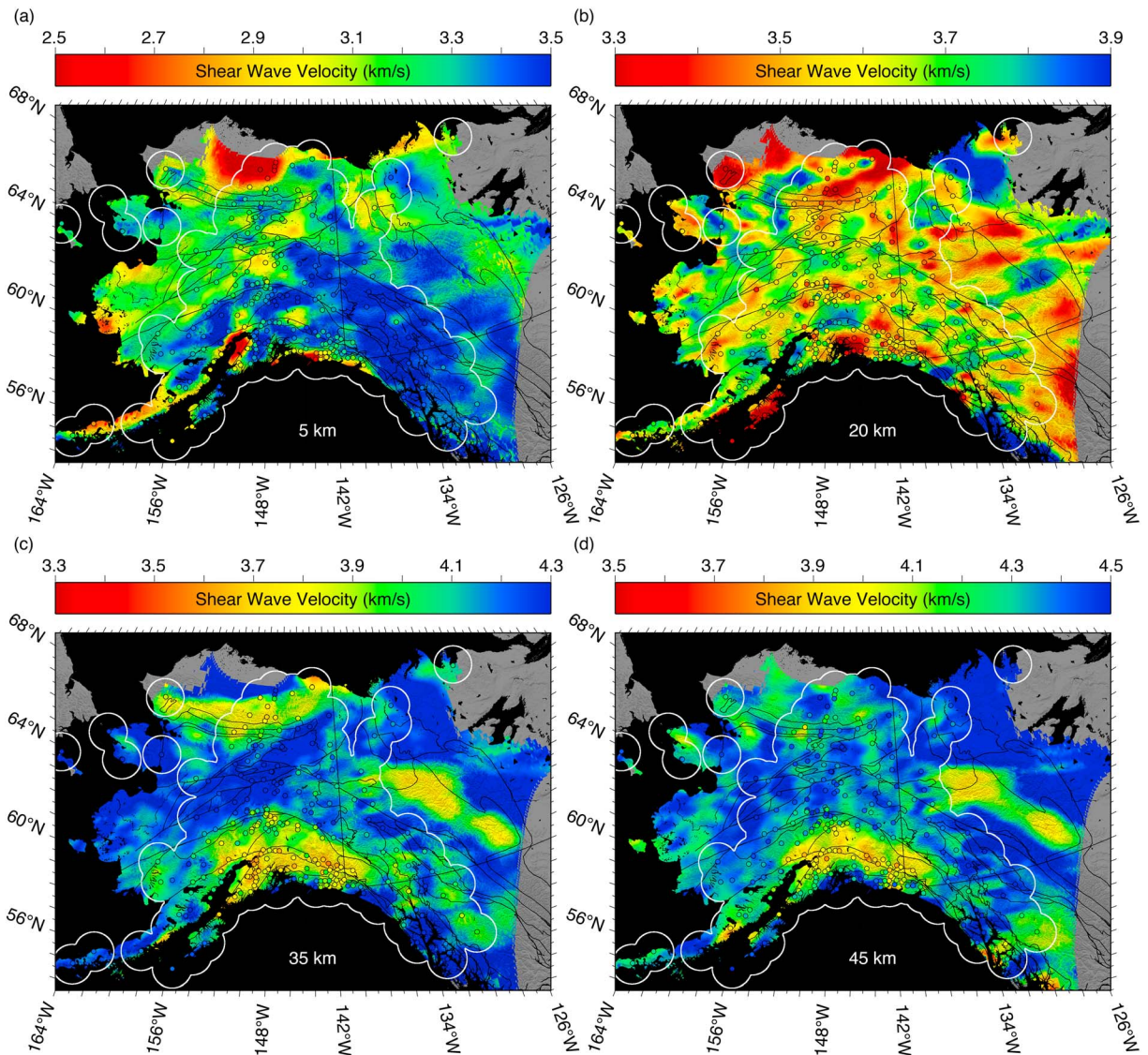
Figure 7. Shear wave velocity results for 5, 20, 35, and 45 km depth (bsl). The colored circles show the shear wave velocity from the 1-D joint receiver function and surface wave inversions results, whereas the maps show the final 3-D surface wave only shear wave inversion results (see main text for difference). The black lines show major terrane boundaries (Colpron et al., 2007). The 5-km depth map highlights basins across our study area (e.g., low shear wave velocities), whereas the 35-km depth map highlights the large crustal thickness variations across our study area (e.g., sharp changes in shear wave velocities across terrane boundaries). The white lines contour a 100-km radius from any station used in our receiver function analysis and provide a reference to highlight areas of our model that incorporate both surface wave and receiver function constraints (Figure 4). Note that each part of the figure has a different color palette range.

3.2. Chugach-Prince William Terrane

The Chugach-Prince William Terrane is a Mesozoic through Cenozoic accretionary prism consisting of marine metasedimentary (e.g., Valdez Group) and mélange (e.g., McHugh Complex) units (Trop & Ridgway, 2007, and references therein). South of the Border Ranges fault system, peaks in the Chugach Terrane reach >4 km with steep topography (Figure 1), suggesting focused uplift and exhumation of the syntaxis (Arkle et al., 2013). Our cross-section results show considerable variation/structure with depth and from west-to-east within the terrane (Figure 8). In the Chugach Terrane, velocities within the top 10–15 km are faster than the surrounding crust with an anticlinal structure especially in the western syntaxis (Figures 8a–8c). In the same cross sections, the top of a northward dipping, arcuate low-velocity zone is observed starting at a depth around 15 km. An earlier study using 2-D seismic reflection data (EDGE 301 line) imaged a similar low-velocity feature with arching reflectors (Ye et al., 1997). Subsequent gravity modeling (Mankhemthong et al., 2013) also imaged a thick
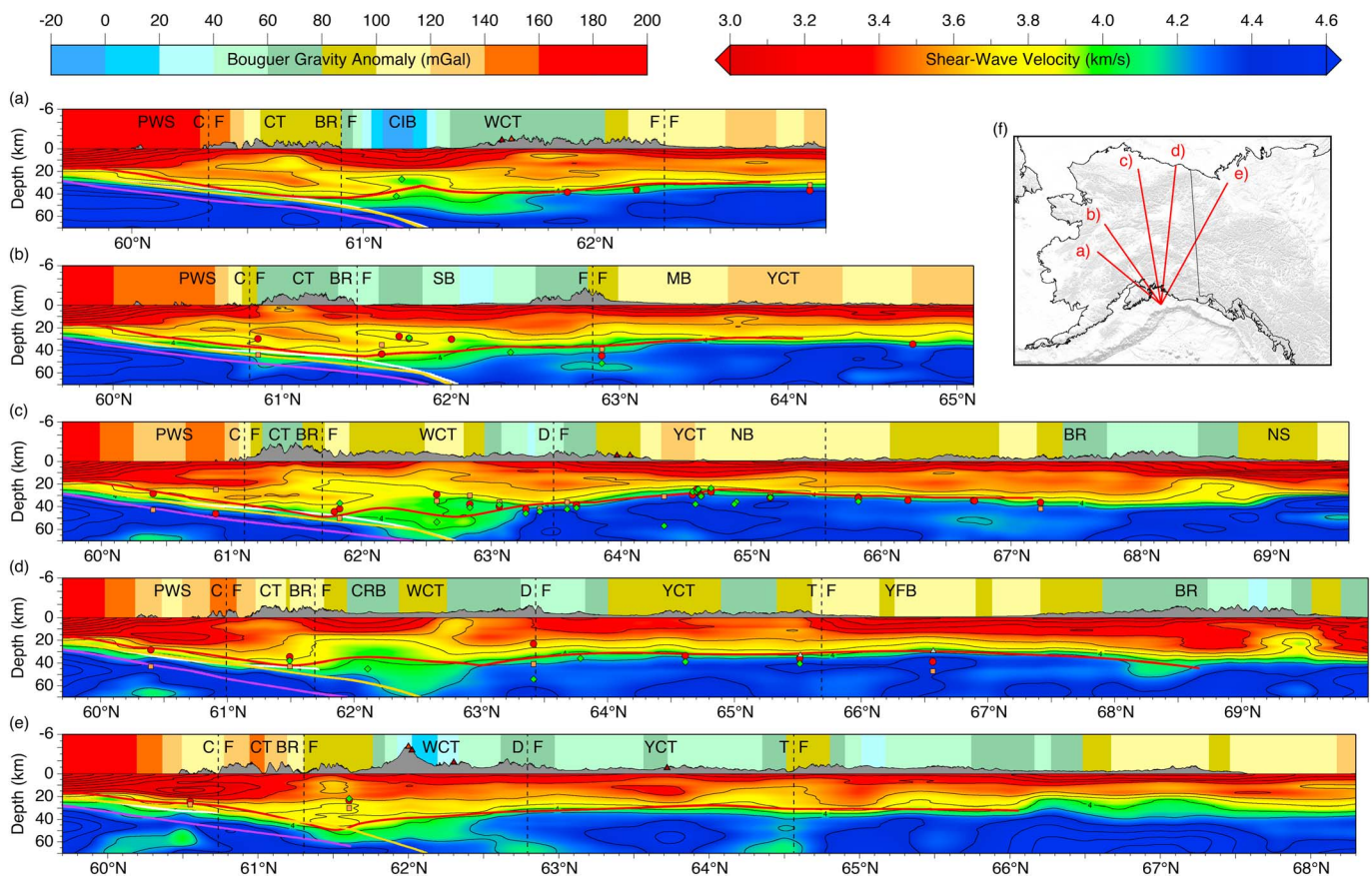
Figure 8. Shear wave velocity results for five cross sections though our model (no vertical exaggeration). (a–e) The same long wavelength (>75 km) Bouguer gravity anomalies from Figure 3 (Bonvalot et al., 2012) are also included and projected onto each cross section behind the vertically exaggerated topography. Major faults acting as terrane boundaries are shown as dashed vertical black lines with major geologic features identified at the top of each cross section. The continental Moho picks from four studies are projected onto our cross-section results and shown as orange squares (IRIS DMC, 2010), green diamonds (Allam et al., 2017), gray triangles (Tarayoun et al., 2017), and red circles (Miller et al., 2018). The continental Moho model generated from a nonperturbational linear surface wave only inversion (Haney et al., 2016) is shown as red lines in the cross sections. The white lines contour the Slab 1.0 slab model (Hayes et al., 2012), and an alternate top of slab model that extends further to the east is also projected onto our cross sections and shown as yellow lines (Pavlis et al., 2018). A slab Moho model corresponding to the top of slab model is also included as purple lines (Pavlis et al., 2018). (f) Map showing the locations of each cross section. PWS, Prince William Sound; CF, Contact Fault; CT, Chugach Terrane; BRF, Border Ranges Fault; CIB, Cook Inlet Basin; WCT, Wrangellia Composite Terrane; FF, Farewell Fault; SB, Susitna Basin; MB, Minchumina Basin; YCT, Yukon Composite Terrane; DF, Denali Fault; NB, Nenana Basin; BR, Brooks Range; NS, North Slope; CRB, Copper River Basin; TF, Tintina Fault; YFB, Yukon Flats Basin.

low-velocity density zone (LDVZ) consistent with the dimensions of the low-velocity feature observed in the reflection data and this study. Both the anticlinal structure in the shallow crust and arcuate low-velocity zone observed in the middle-to-lower crust are no longer visible in the crust east of the Prince William Sound (Figure 8e).

3.3. Wrangellia Composite Terrane

The Wrangellia Composite Terrane and the Alaska Range suture zone are bounded to the north by the Denali fault (Farewell fault in western Alaska) and the south by the Border Ranges fault system (Figure 1). Displacement along the Denali fault varies from ~400 km along the eastern segment (mostly dextral strike slip) to ~100 km along the western segment (larger component of thrusting; Fitzgerald et al., 2014, and references therein), whereas the Border Ranges fault system has ~130 km of accumulated dextral strike slip (Pavlis & Roeske, 2007). Thick fore arc (e.g., Cook Inlet) and intermontane (e.g., Copper River) basins with high-elevation transpressional (e.g., Alaska Range) and arc volcanic (e.g., Wrangell Volcanic Field) peaks provide evidence of both the complex terrane assembly and active subduction zone tectonics. Aside from the basin signatures (e.g., Cook Inlet, Susitna, and Copper River), the middle-to-upper crust is faster to the south and
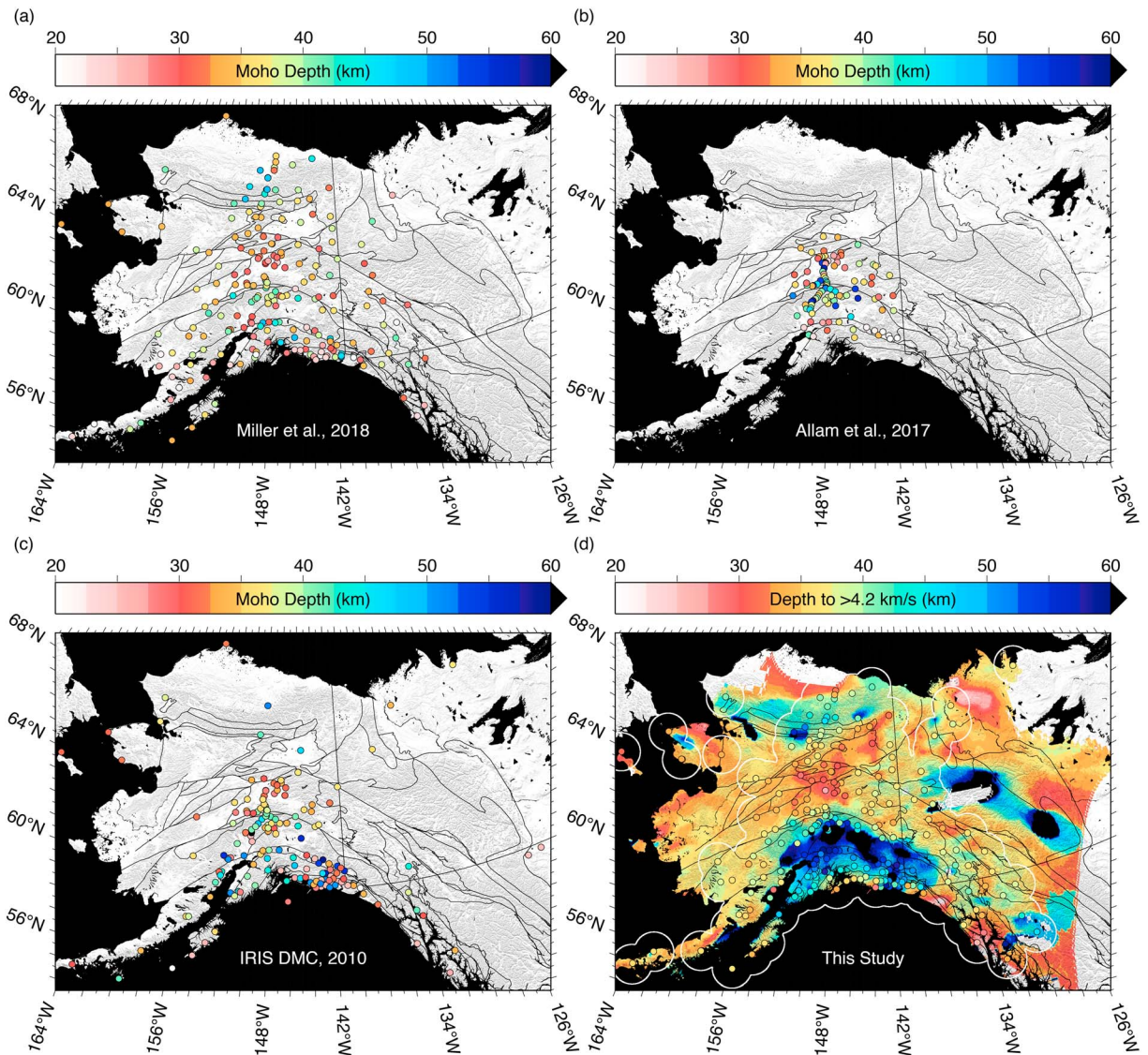
Figure 9. (a–c) Moho depth estimates from three studies (Allam et al., 2017; IRIS DMC, 2010; Miller et al., 2018). (d) The colored circles show the depth where our shear wave velocity model exceeds 4.2 km/s from the 1-D joint receiver function and surface wave inversions results, whereas the map shows the depth where the final 3-D surface wave only shear wave inversion results exceeds 4.2 km/s (see main text for difference). We note that this figure only approximates the Moho depth at some locations and is intended as a qualitative proxy for comparison with other Moho depth estimates.

slower to the north and west in our velocity model. Previous studies have imaged a highly variable crustal thickness beneath the terrane with the thickest crust existing beneath the northernmost Alaska Range suture zone (Allam et al., 2017; Brennan et al., 2011; Fuis et al., 2008; Miller et al., 2018; Veenstra et al., 2006). From just our shear wave velocity results, it is difficult to assign a crustal thickness. However, we observe velocities typically associated with crustal compositions (<4.2 km/s) up to 70-km depth (about as deep as our model has resolution) that are thickest further to the south along the top of the subducting pacific plate thinning to the north under the Denali fault (Figures 8 and 9). These depths are inconsistent with previous crustal thickness estimates, and the tectonic significance of these observations is discussed in the following section.

3.4. Yukon Composite Terrane

The Yukon Composite Terrane is composed primarily of the Yukon-Tanana Terrane, which experienced mid-Cretaceous extension exposing highly extended metamorphosed continental crust (Pavlis et al., 1993), along

with other variably metamorphosed continental margin assemblages. The northern extent of the Yukon Composite Terrane is bounded by the dextral Tintina fault with ~400 km of dextral strike slip in the east (Tempelman-Kluit, 1976). However, lowland areas that extend beyond terrane boundaries define much of interior Alaska and the northern extent of the composite terrane in the west is more diffuse. Previous studies have imaged a significant transition in crustal thickness between the Wrangellia Composite Terrane and the Yukon Composite Terrane (Fuis et al., 2008; Miller et al., 2018; Veenstra et al., 2006) with some studies suggesting that the Moho offset across the Hines Creek fault might be quite sharp (~10 km of vertical offset; e.g., Allam et al., 2017 ; Brennan et al., 2011 ; Rossi et al., 2006). Although our shear wave model reaches velocities typically associated with mantle compositions (>4.2 km/s) at much shallower depths in the Yukon Composite Terrane than the Wrangellia Composite Terrane (Figures 7c, 8, and 9d), our processing scheme would smooth any sharp lateral velocity offsets. We also observe a rather consistent velocity profile on either side of the Denali and Hines Creek faults that extends laterally beyond the effects of our smoothing. This observation is consistent with previous imaging studies that show a similar velocity profile across the terranes (Allam et al., 2017; Fuis et al., 2008; McLellan et al., 2018).

3.5. Northern Alaska (Brooks Range)

Northern Alaska is a mosaic of terranes accreted and constructed through various deformation styles (Colpron et al., 2007). The most recent and dominant in terms of crustal deformation and topographic signature has been the thick and thin-skinned fold-and-thrust belts of the Arctic Alaska Terrane. Paleocene and Eocene shorting resulted in thick-skinned deformation in the Brooks Range that transitioned into thin-skinned deformation of the Cretaceous Colville foreland basin (Moore & Box, 2016). At the time of this study, stations were only available in eastern northern Alaska (United States) and westernmost Yukon (Canada); thus, our results are limited to those parts of the Northern Cordillera. However, where our results are well constrained in northern Alaska (Figures 8c and 8d), we observe similar results to previous studies in the area. For example, velocities in our model typically associated with crustal compositions (<4.2 km/s) gradually thicken from ~30 km at the Tintina fault to a maximum depth around ~40 km under the high-topography Brooks Range rapidly shallowing again to ~30 km under the North Slope (Figure 8c). This crustal thickness trend has been observed before (Fuis et al., 2008; Miller et al., 2018) and is consistent with the crustal thickness predicted by the topography. Perhaps more interesting is the crustal structure beneath the northern Brooks Range (Cenozoic thin-skinned fold-and-thrust deformation) where we observe a south dipping wedge of faster crustal material in the middle-to-lower crust (Figure 8c), also observed in previous studies (Fuis et al., 2008).

4. Discussion

The following discussion is not indented to be an exhaustive description of our tomography model and the features we observe. Rather, we discuss a few prominent observations that our Cordillera-scale results highlight and try and place them in the context of existing studies. A major focus of our discussion is how integration of our new tomography results with previous geophysical and geological studies can help refine existing tectonic interpretations as well as provide new directions for future investigation.

4.1. Uplift of the Chugach Mountains

The most prominent low-velocity zone we image in our results is located in the midcrust beneath the Chugach Terrane starting at depths around 10–15 km (Figures 8a–8c). Previous 2-D studies have imaged a similar low-velocity feature with arching reflectors (Ye et al., 1997) and modeled a low-density anomaly from gravity measurements (Mankhemthong et al., 2013) consistent with the top of the low-velocity feature observed in this study. However, both the seismic refraction and gravity modeling studies show the low-velocity, low-density structure is a continuous feature from ~10- to 15-km depth to the top of the slab (30–40 km), whereas the low-velocity feature we image appears to be confined to the mid-crust (Figures 8a–8c). This apparent discrepancy between our model and previous studies is resolved when existing models are examined in more detail. Although the low-density anomaly is modeled as a homogeneous body (i.e., constant density), the seismic velocities from the refraction study show a 15% P wave velocity increase from the top of the anomaly to the bottom (Ye et al., 1997). Assuming the Vp/Vs ratio does not change significantly over this depth range in the anomaly, a 15% increase of the velocities at the top of our imagined low-velocity zone (~10–15 km) are consistent with the velocities on top of the slab defined

by the Slab 1.0 contour (Hayes et al., 2012) beneath the low-velocity anomaly in our model. Thus, we suggest that the low-velocity zone we observe in our results beneath the Chugach Mountains corresponds to the top of a low-velocity, low-density body interpreted by previous studies as underplated sediments (e.g., Arkle et al., 2013; Buscher et al., 2008; Mankhemthong et al., 2013; Ye et al., 1997).

Whereas previous studies have imaged or modeled the 2-D arcuate geometry of the underplated sediments, the along-strike distribution remains somewhat poorly constrained. For example, the seismic refraction line (Ye et al., 1997) was a marine survey off the Kodiak shelf ~275 km southwest of the relatively narrowly confined gravity anomaly interpreted as underplated sediments in the western Chugach Mountains (Mankhemthong et al., 2013). The same gravity modeling does not require any low-density body southwest of the northern Cook Inlet (Kenai Mountains) to satisfy the gravity anomaly data. This suggests that >20-km-thick and ~100-km-wide (downdip length) underplated sediments are a relatively discontinuous feature along this section of the subduction zone interface. An alternate explanation is that the gravity modeling results are highlighting density heterogeneities within a continuous along-strike feature that extends laterally further to the southwest.

Our 3-D velocity model allows us to see how this low-velocity anomaly varies along the trend of the Chugach Terrane. Although our model resolution is limited around the offshore area of the seismic refraction line, we observe a continuous low-velocity zone as far to the southwest as the Kenai Peninsula and as far to the east as the cross section that traverses the center of the Prince William Sound (Figure 8c). If the low-velocity anomaly we observe in our results is correctly associated with underplated sediments along the subduction zone interface, it would exist not only under both areas with rapid exhumation rates in the western Chugach Mountains (Arkle et al., 2013) but also beneath areas that are below sea level (Ye et al., 1997). This suggests that the presence of underplated sediments alone may not be sufficient to explain the rapid uplift and exhumation rates of the western Chugach Mountains. Future studies with higher resolution and a narrower focus may be able to detect subtler features of the low-velocity anomaly and further refine our understating of the uplift mechanisms in the Chugach.

4.2. Cordilleran Crustal Thickness

From south to north, our tomographic images show crustal velocities (<4.2 km/s) at deeper depths under the Wrangellia Composite Terrane south of the Denali fault that rapidly shallow under interior Alaska, gradually deepen under the Brooks Range before shallowing again under the North Slope (Figures 7c, 8c, and 9). This crustal thickness pattern has been observed previously in 2-D cross sections (e.g., Fuis et al., 2008) and a series of 1-D crustal thickness estimates (e.g., Miller et al., 2018; O'Driscoll & Miller, 2015). Although we do not invert for a specific Moho model parameter, the addition of the receiver function data in the inversion constrains discontinuities better than surface wave inversions alone (Ward et al., 2014, supporting information). Therefore, we attribute these variations in our velocity model primarily to variations in crustal thickness.

An advantage of our velocity model is the ability to evaluate large-scale crustal thickness variations in 3-D. A qualitative example of this comes from a comparison of our 35-km depth slice (Figure 7c) or depth to 4.2-km/s map (Figure 9d) with the long wavelength (>75 km) Bouguer gravity anomaly map (Figure 3). We have chosen our shear wave velocity color palette so that blue regions (>4.2 km/s) are almost certainly in the mantle. Assuming the long wavelength (>75 km) Bouguer gravity anomaly map is mostly sensitive to crustal thickness variations (with a few exceptions from subduction zone effects and thick basin sediments), a particularly striking correlation is observed between an irregular area of relatively high gravity (Figure 3) and mantle velocities (Figure 7c) across the Alaska interior lowlands. The correlation is equally impressive with areas of relatively low gravity matching the location of crustal velocities in the accreted terranes south of the Denali fault, in the Yukon-Tanana uplands, and in the arcuate Brooks Range. This qualitative comparison suggests that our velocity model is imaging 3-D crustal thickness variations consistent with the long wavelength (>75 km) Bouguer gravity anomaly map. However, a more detailed and quantitative comparison of our velocity model with existing 1-D crustal thickness estimates can help refine those models while providing insightful tectonic context for our interpretations.

Our final velocity model is constructed from both surface wave data and receiver functions where available. Therefore, we expect some agreement with previous 1-D crustal thickness estimates based on receiver function imaging alone. Three recent receiver function studies have made available in digital format their crustal

thickness estimates for direct comparison with our velocity model (Allam et al., 2017; IRIS DMC, 2010; Miller et al., 2018). We note that all three studies use radial receiver functions to image the Moho; however, each study uses a slightly different approach to extract Moho estimates from the receiver functions. The IRIS DMC EarthScope Automated Receiver Survey (Crotwell & Owens, 2005) uses the automated method of H-K stacking (interface depth-*Vp/Vs* ratio), assuming the interface with the maximum amplitude is the Moho (Zhu & Kanamori, 2000). More recent studies stack receiver functions from the same station (after a slowness correction) and migrate the stack from time to depth using a 1-D (Miller et al., 2018) or 3-D (Allam et al., 2017) velocity model from which a Moho conversion depth is manually selected. Using many of the same stations and data, some Moho picks from these studies are more than 10 km different, while others are within meters of each other. This is not intended to be a criticism, but rather highlights the advantages/disadvantages of using only receiver functions to image the Moho and the utility of comparison with our velocity model. The continental Moho picks from these studies are projected onto our cross-section results (Figure 8) as orange squares (IRIS DMC, 2010), green diamonds (Allam et al., 2017), and red circles (Miller et al., 2018) as well as included in separate map view plots (Figures 9a–9c).

We also compare our final velocity model with a continental Moho model generated from a nonperturbational linear surface wave only inversion (Haney & Tsai, 2015). The Moho model was generated using a new underparameterized version of a Dix-type relation for a layer over a half-space (Haney et al., 2016). The continental Moho model from the previous Dix-type inversion study is projected onto our cross-section results as a red line (Figure 8). Typically, surface waves alone are not particularly well suited to imaging the Moho or other sharp discontinuities because of their broad sensitivity kernels. However, we observe rather good agreement with the continental Moho model and Moho picks from the receiver function only studies in areas where the current tectonic setting is less complex (Figure 8). The crust-mantle transition beneath the Wrangellia Composite Terrane is considerably more complex than the rest of our study area and is where we observe the poorest agreement between our velocity model and previous Moho depth models (Figure 9d). The nature of the crust and uppermost mantle beneath the Wrangellia Composite Terrane (mantle wedge) is discussed in the following section.

4.3. Nature of the Mantle Wedge

The complex nature of the crust and uppermost mantle beneath the Wrangellia Composite Terrane (particularly in the fore arc) is strikingly evident when multiple seismic results and surfaces are plotted on top of our tomography model (Figure 8). If we assume the ~4.2-km/s velocity contour as a proxy for the crust-mantle transition in our tomography results, at least one of the continental Moho picks (Allam et al., 2017; IRIS DMC, 2010; Miller et al., 2018) and the continental Moho model surface (Haney et al., 2016) fall within ±2 km of the 4.2-km/s velocity contour with only two exceptions. The first exception is located in the Yukon Flats Basin (Figure 8d), and this is easily attributed to basin effects and contamination from shallow multiples. For this reason, stations located in the Yukon Flats Basin did not pass our initial quality control selection criteria and were not used in our receiver function analysis. Nevertheless, the discrepancy between the 4.2-km/s velocity contour and previous continental Moho estimates are still within ~5 km at this location.

The second exception is located in the fore arc of the Wrangellia Composite Terrane (Figures 8 and 9) where the discrepancy between the 4.2-km/s velocity contour and previous continental Moho estimates are significantly larger (>10 km). The deviation of the continental Moho model surface (Haney et al., 2016) from both the 4.2-km/s velocity contour and previous continental Moho picks under the fore arc of the Wrangellia Composite Terrane is relatively easy to explain. The generation of the continental Moho model surface assumes a layer over a half-space (Haney & Tsai, 2015), which works well to the south (i.e., continental fore arc over the subducting slab) and to the north (i.e., continental crust over the mantle). The presence of a thin mantle wedge under the Wrangellia Composite Terrane violates the simple assumption of a layer over a half-space, and the inversion effectively splits the difference between the continental Moho and the top of the subducting slab. The deviation of the continental Moho picks (Allam et al., 2017; IRIS DMC, 2010; Miller et al., 2018) from the 4.2-km/s velocity contour is, however, not as easily explained unless the nature of the crust-mantle transition above the wedge is significantly different from the rest of our study area.

One possible explanation for the discrepancy between the 4.2-km/s velocity contour and previous continental Moho estimates is that the crust is considerably thicker than existing Moho estimates for this area. For example, Fuis et al. (2008) interpreted a thick crustal section (<55 km) beneath the Peninsular Terrane

(southernmost Wrangellia Composite Terrane) as a section of accreted island arc crust along our cross section shown in Figure 8d. However, there are not many Moho picks in this area to compare with our tomography results, and therefore, we cannot uniquely extend this interpretation to account for the discrepancy between the 4.2-km/s velocity contour and previous continental Moho estimates along the strike of the mantle wedge. Additionally, the 4.2-km/s velocity contour extends far below the maximum interpreted depth (~55 km) of the accreted island arc crust and is still not a viable alternate explanation for the depth of the relatively low velocities in our tomography results in the mantle wedge. The results of an active USArray Flex Array experiment (Christensen & Abers, 2016) in the area at the time of our study with denser station coverage might further refine this ambiguity. However, based on our current tomography results and previous studies, we favor a shallower crust-mantle transition as seen by existing Moho picks especially since several (>10) stations from multiple studies (Allam et al., 2017; IRIS DMC, 2010; Miller et al., 2018) image a similar Moho depth over the mantle wedge. Assuming the existing Moho picks are accurately locating the crust-mantle transition, their integration with our tomography results suggests that the nature of the mantle wedge is significantly different from the rest of the sub-Moho mantle across the Alaskan Cordillera.

This interpretation is consistent with several previous mantle tomography studies that have imaged a low-velocity mantle wedge (e.g., Eberhart-Phillips et al., 2006; Tian & Zhao, 2012; Wang & Tape, 2014) with high seismic attenuation (Stachnik et al., 2004). An advantage of our tomography model over previous tomography models is a higher resolution tomographic image extending along the entire oceanic-continental mantle wedge. To further highlight this low-velocity mantle wedge in our tomography results, we have extracted the shear wave velocity results from our model corresponding to the Moho depths from Miller et al. (2018) and plotted them in Figure 10. Moho estimates that extend beneath the Slab 1.0 (Hayes et al., 2012) or top-of-slab (Pavlis et al., 2018) models have been removed and are not shown. In general, faster velocities (>4.0 km/s) at the Moho are observed North of the mantle wedge with significantly slower velocities (<4.0 km/s) observed at the crust-mantle transition in the mantle wedge. Furthermore, there is no systematic relationship between the depths of the Moho estimates, terrane boundaries, or projected extent of the subducted Yakutat Terrane and the low velocities observed at the crust-mantle transition in the fore arc of the Wrangellia Composite Terrane. There is, however, a correlation with the 80-km contour from the top-of-slab model (Pavlis et al., 2018) that delineates the majority of slower velocities (<4.0 km/s) observed at the crust-mantle transition. This is in excellent agreement with a previous study that estimated as much as 30% serpentinization of the mantle wedge where the slab is <80-km deep (Rossi et al., 2006). Thus, our results are consistent with previous studies that have interpreted this feature as a region of serpentinized mantle.

However, recent global compilations have begun to question the degree to which the mantle wedge is serpentinized in subduction zones, although it has long been argued that ample geological and geophysical evidence exists for the presence extensive serpentinization in the fore-arc mantle (Hyndman & Peacock, 2003). For example, Ji et al. (2013) estimated that many of the mantle wedges in subduction zones on Earth have a significant and often underestimated amount (>50%) of serpentinization based primarily on seismic velocities. Conversely, Abers et al. (2017) augured from thermal modeling results that dehydration of the subducting slab is too slow to hydrate (i.e., serpentinize) the cold mantle wedge in all but the hottest subduction zones (e.g., Cascadia). Abers et al. (2017) also suggest that many of the low-velocity cold mantle wedges have been misinterpreted as serpentinized mantle or, at the very least, the percentage of serpentinization has been overestimated. A corollary of this conclusion is that an alternate explanation for the low velocities observed in the mantle wedge is required. The most likely explanations involve a variety of subduction zone processes that contaminate the mantle wedge with crustal velocity material and lower the bulk mantle wedge velocity without serpentinization (Abers et al., 2017, and reference therein).

Based on the above information, our velocity model results alone cannot uniquely establish the percentage of serpentinization, or even the presence/absence of any mantle hydration beneath the Wrangellia Composite Terrane fore arc. However, we can broadly assume that the low velocities in the mantle wedge we observe beneath the continental crust are related to the effects of a downgoing slab. This is significant because we observe a low-velocity mantle wedge east of the seismicity typically used to define the eastern edge of the subducting Pacific plate or subducted Yakutat Terrane. The presence of a downgoing slab east of the seismicity (Figure 2) is consistent with an alternate slab model first presented by Bauer et al. (2014), later extended by Pavlis et al. (2018), and imaged by Jiang et al. (2018). We note that the low-velocity mantle
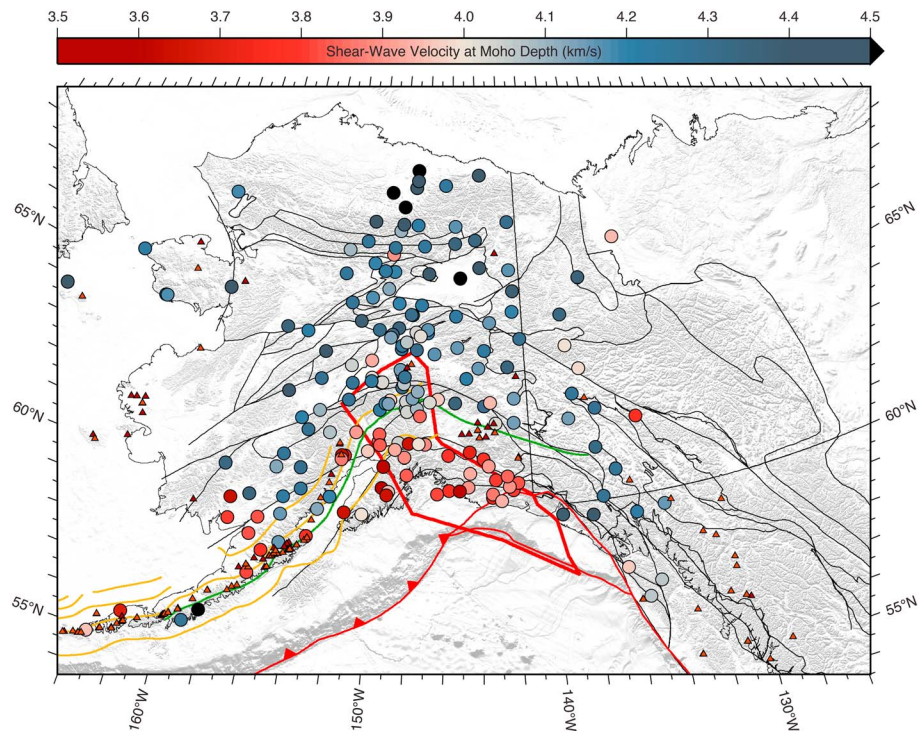
Figure 10. Shear wave velocities from our model at the depth of the continental Moho presented by Miller et al. (2018). Moho estimates with offsets greater than 10 km of nearby stations or deeper than the top-of-slab model (Pavlis et al., 2018) are removed in this plot. Holocene volcanic activities from the Smithsonian Institution Global Volcanism Program are shown as red triangles, and the dark red triangles show older (<2 Ma) volcanic activity from the Alaska Volcano Observatory. The black lines show major terrane boundaries (Colpron et al., 2007), the green line contours the 80 km to top-of-slab model (Pavlis et al., 2018), and the gold lines contour the Slab 1.0 slab model (Hayes et al., 2012). The above surface expression and projected extent of the subducted Yakutat Terrnae is shown as the irregular polygon with thick red lines (Eberhart-Phillips et al., 2006). Note that the stations with slow shear wave velocities (<4.0 km/s, red) at the Moho and also in the sub-Moho mantle are not strictly confined by any specific terrane/fault boundary or by the projected extent of the subducted Yakutat Terrane.

wedge in general follows this alternate slab model (Figure 8, yellow lines) especially well considering no slab interface (or Moho interface) has been prescribed in our inversion scheme. If such an aseismic slab is subducting beneath the eastern Wrangellia Composite Terrane, it provides a simple explanation for the location of the active Wrangell arc volcanoes. It also elicits additional questions such as why this section of the slab is aseismic and why previous tomography studies have not observed a slab feature east of the seismicity (Figure 2). Future mantle tomography studies that utilize the entire Earthscope seismic array may help answer some of these outstanding tectonic questions.

5. Conclusions

In this study, we used broadband seismic data from the USArray TA (June 2014 through May 2017) to generate Rayleigh wave phase velocity maps (8–40 s). In addition to the USArray data, we calculated radial receiver functions from existing temporary and permanent seismic networks (May 1999 through May 2017). The receiver functions were jointly inverted with the surface wave dispersion data for a 3-D shear wave velocity model across the Alaskan Cordillera with a maximum depth resolution around 70 km. Large-scale features of our shallow velocity model agree with the locations of large sedimentary basins (Kirschner, 1988; Moore & Box, 2016), and our intermediate depth results are generally consistent with previous 1-D (Rossi et al., 2006) and 2-D (Fuis et al., 2008) Moho estimates. Our detailed 3-D velocity model allows us to track the lateral extent of a low-velocity, low-density zone interpreted by previous studies (Arkle et al., 2013; Mankhemthong et al., 2013) as underplated sediments responsible for the rapid uplift of the Chugach Mountains. Integration of our velocity model with existing Moho estimates (Allam et al., 2017; Haney et al., 2016; IRIS DMC, 2010; Miller et al.,

2018; Tarayoun et al., 2017) allows us to directly evaluate these models while simultaneously validating anomalous and unexpected features in our velocity model. One such notably anomalous and unexpected feature in our results is a laterally extensive low-velocity mantle wedge. Although we cannot uniquely interpret the nature of this feature, we suggest that it results from the effects of a downgoing slab that is continuous further to the east than the seismicity would predict. We acknowledge this interpretation remains somewhat speculative at this time; however, future studies that incorporate the entire TA as well as existing data sets (including our velocity model) may further refine/reject this interpretation.

References

Abers, G., & Christensen, D. (2006). Multidisciplinary observations of subduction. International Federation of Digital Seismograph Networks. Other/Seismic Network. doi:10.7914/SN/YV_2006

Abers, G. A., van Keken, P. E., & Hacker, B. R. (2017). The cold and relatively dry nature of mantle forearcs in subduction zones. *Nature Geoscience*, 10(5), 333–337. https://doi.org/10.1038/ngeo2922

Alaska Earthquake Center, Univ. of Alaska Fairbanks (1987). Alaska regional network. International Federation of Digital Seismograph Networks. Other/seismic network. doi:10.7914/SN/AK

Albuquerque Seismological Laboratory (ASL)/USGS (1990). United States National Seismic Network. International Federation of Digital Seismograph Networks. Other/seismic network. doi:10.7914/SN/US

Allam, A. A., Schulte-Pelkum, V., Ben-Zion, Y., Tape, C., Ruppert, N., & Ross, Z. (2017). Ten kilometer vertical Moho offset and shallow velocity contrast along the Denali fault from double-difference tomography, receiver functions, and fault zone head waves. *Tectonophysics*, 721, 56–69. https://doi.org/10.1016/j.tecto.2017.09.003

Arkle, J. C., Armstrong, P. A., Haeussler, P. J., Prior, M. G., Hartman, S., Sendziak, K. L., & et al. (2013). Focused exhumation in the syntaxis of the western Chugach Mountains and Prince William Sound, Alaska. *Geological Society of America Bulletin*, 125(5–6), 776–793. https://doi.org/10.1130/B30738.1

Barmin, M. P., Ritzwoller, M. H., & Levshin, A. L. (2001). A fast and reliable method for surface-wave tomography. *Pure and Applied Geophysics*, 158(8), 1351–1375. https://doi.org/10.1007/PL00001225

Bauer, M. A., Pavlis, G. L., & Landes, M. (2014). Subduction geometry of the Yakutat terrane, southeastern Alaska. *Geosphere*, 10(6), 1161–1176. https://doi.org/10.1130/GES00852.1

Bensen, G. D., Ritzwoller, M. H., Barmin, M. P., Levshin, A. L., Lin, F., Moschetti, M. P., et al. (2007). Processing seismic ambient noise data to obtain reliable broad-band surface wave dispersion measurements. *Geophysical Journal International*, 169(3), 1239–1260. https://doi.org/10.1111/j.1365-246X.2007.03374.x

Bonvalot, S., Balmino, S., Briais, A., Kuhn, M., Peyrefitte, A., & Vales, N. (2012). *World gravity map, Bureau Gravimetrique International (BGI)*. Paris: CGMW-BGI-CNES-IRD.

Brennan, P. R. K., Gilbert, H., & Ridgway, K. D. (2011). Crustal structure across the central Alaska range: Anatomy of a Mesozoic collisional zone. *Geochemistry, Geophysics, Geosystems*, 12, Q04010. https://doi.org/10.1029/2011gc003519

Buscher, J. T., Berger, A. L., & Spotila, J. A. (2008). Exhumation in the Chugach-Kenai mountain belt above the Aleutian subduction zone, southern Alaska. In J. Freymueller et al. (Eds.), *Active Tectonics and Seismic Potential of Alaska, Geophysical Monograph Series* (Vol. 179, pp. 151–166). Washington, DC: American Geophysical Union. https://doi.org/10.1029/179GM08

Christensen, D., & Abers, G. (2016), Fate and consequences of Yakutat terrane subduction beneath eastern Alaska and the Wrangell volcanic field. International Federation of Digital Seismograph Networks. Other/Seismic Network doi:10.7914/SN/YG_2016

Christensen, D., Hansen, R., & Abers, G. (1999), Broadband experiment across the Alaska range. International Federation of Digital Seismograph Networks. Other/Seismic Network. doi:10.7914/SN/XE_1999

Colpron, M., Nelson, J. L., & Murphy, D. C. (2007). Northern cordilleran terranes and their interactions through time. *GSA Today*, 17(4), 4–10. https://doi.org/10.1130/GSAT01704-5A.1

Crotwell, H. P., & Owens, T. J. (2005). Automated receiver function processing. *Seismological Research Letters*, 76(6), 702–709. https://doi.org/10.1785/gssrl.76.6.702

Eberhart-Phillips, D., Christensen, D. H., Brocher, T. M., Hansen, R., Ruppert, N. A., Haeussler, P. J., & et al. (2006). Imaging the transition from Aleutian subduction to Yakutat collision in Central Alaska, with local earthquakes and active source data. *Journal of Geophysical Research*, 111, B11303. https://doi.org/10.1029/2005JB004240

Fitzgerald, P. G., Roeske, S. M., Benowitz, J. A., Riccio, S. J., Perry, S. E., & Armstrong, P. A. (2014). Alternating asymmetric topography of the Alaska Range along the strike-slip Denali fault: Strain partitioning and lithospheric control across a terrane suture zone. *Tectonics*, 33, 1519–1533. https://doi.org/10.1002/2013TC003432

Fuis, G. S., Moore, T. E., Plafker, G., Brocher, T. M., Fisher, M. A., Mooney, W. D., et al. (2008). Trans-Alaska crustal transect and continental evolution involving subduction underplating and synchronous foreland thrusting. *Geology*, 36(3), 267–270. https://doi.org/10.1130/G24257A.1

Geological Survey of Canada (1989). Canadian National Seismograph Network. International Federation of Digital Seismograph Networks. Other/seismic network. doi:10.7914/SN/CN

Haney, M. M., & Tsai, V. C. (2015). Nonperturbational surface-wave inversion: A dix-type relation for surface waves. *Geophysics*, 80(6), EN167–EN177. https://doi.org/10.1190/geo2014-0612.1

Haney, M. M., Tsai, V. C., & Ward, K. M. (2016). Widespread imaging of the lower crust, Moho, and upper mantle from Rayleigh waves: A comparison of the Cascadia and Aleutian-Alaska subduction zones, abstract T11D-2645, presented at 2016 fall meeting, AGU, San Francisco, Calif., 12-16 Dec.

Hayes, G. P., Wald, D. J., & Johnson, R. L. (2012). Slab1.0: A three-dimensional model of global subduction zone geometries. *Journal of Geophysical Research*, 117, B01302. https://doi.org/10.1029/2011JB008524

Herrmann, R. B., & Ammon, C. J., (2004). Herrmann: Computer programs in seismology-surface waves, receiver functions and crustal structure. Saint Louis University. [Available at http://www.eas.slu.edu/People/RBHerrmann/ComputerPrograms.html].

Hutko, A. R., Bahavar, M., Trabant, C., Weekly, R. T., Van Fossen, M., & Ahern, T. (2017). Data products at the IRIS-DMC: Growth and usage. *Seismological Research Letters*, 88(3), 892–903. https://doi.org/10.1785/0220160190

Hyndman, R. D., & Peacock, S. M. (2003). Serpentinization of the forearc mantle. *Earth and Planetary Science Letters*, 212, 417–432.

IRIS DMC (2010). Data services products: EARS EarthScope automated receiver survey. doi:10.17611/DP/EARS.1

IRIS Transportable Array (2003). USArray transportable array. International Federation of Digital Seismograph Networks. Other/Seismic Network. doi:10.7914/SN/TA

Ji, S., Li, A. W., Wang, Q., Long, C. X., Wang, H. C., Marcotte, D., & et al. (2013). Seismic velocities, anisotropy, and shear-wave splitting of antigorite serpentinites and tectonic implications for subduction zones. *Journal of Geophysical Research: Solid Earth*, *118*, 1015–1037. https://doi.org/10.1002/jgrb.50110

Jiang, C., Schmandt, B., Ward, K. M., Lin, F., & Worthington, L. L. (2018). Upper mantle seismic structure of Alaska from Rayleigh and S-wave tomography. *Geophysical Research Letters*, *45*. https://doi.org/10.1029/2018GL079406

Julià, J., Ammon, C. J., Herrmann, R. B., & Correig, A. M. (2000). Joint inversion of receiver function and surface wave dispersion observations. *Geophysical Journal International*, *143*(1), 99–112. https://doi.org/10.1046/j.1365-246x.2000.00217.x

Kirschner, C. E. (1988). Map showing sedimentary basins of onshore and continental shelf areas, Alaska: U.S. Geological Survey Miscellaneous Investigations Series Map 1873, 1 sheet, scale 1:2,500,000.

Langston, C. A. (1979). Structure under Mount Rainier, Washington, inferred from teleseismic body waves. *Journal of Geophysical Research*, *84*(B9), 4749–4762. https://doi.org/10.1029/JB084iB09p04749

Ligorria, J. P., & Ammon, C. J. (1999). Iterative deconvolution and receiver-function estimation. *Bulletin of the Seismological Society of America*, *89*(5), 1395–1400.

Lin, F. C., Moschetti, M. P., & Ritzwoller, M. H. (2008). Surface wave tomography of the western United States from ambient seismic noise: Rayleigh and Love wave phase velocity maps. *Geophysical Journal International*, *173*(1), 281–298. https://doi.org/10.1111/j.1365-246X.2008.03720.x

Mankhemthong, N., Doser, D. I., & Pavlis, T. L. (2013). Interpretation of gravity and magnetic data and development of two-dimensional cross-sectional models for the Border Ranges fault system, south-central Alaska. *Geosphere*, *9*(2), 242–259. https://doi.org/10.1130/GES00833.1

McLellan, M., Schaeffer, A. J., & Audet, P. (2018). Structure and fabric of the crust and uppermost mantle in the northern Canadian Cordillera from Rayleigh-wave tomography. *Tectonophysics*, *724-725*, 28–41. https://doi.org/10.1016/j.tecto.2018.01.011

Miller, M. S., O'Driscoll, L. J., Porritt, R. W., & Roeske, S. M. (2018). Multiscale crustal architecture of Alaska inferred from P receiver functions. *Lithosphere*, *10*(2), 267–278. https://doi.org/10.1130/L701.1

Moore, T. E., & Box, S. E. (2016). Age, distribution and style of deformation in Alaska north of 60°N: Implications for assembly of Alaska. *Tectonophysics*, *691*, 133–170. https://doi.org/10.1016/j.tecto.2016.06.025

NOAA National Oceanic and Atmospheric Administration (USA) (1967). National Tsunami Warning Center Alaska Seismic Network. International Federation of Digital Seismograph Networks. Other/seismic network. doi:10.7914/SN/AT

O'Driscoll, L. J., & Miller, M. S. (2015). Lithospheric discontinuity structure in Alaska, thickness variations determined by Sp receiver functions. *Tectonics*, *34*, 694–714. https://doi.org/10.1002/2014TC003669

Pavlis, G. L., Bauer, M. A., Elliott, J. L., Koons, P., Pavlis, T. L., Ruppert, N., et al. (2018). Data Supplement for Alaska Lithospheric Model Data Files. https://doi.org/10.5967/K8QC01N6

Pavlis, T. L., & Roeske, S. M. (2007). The border ranges fault system, southern Alaska, in special paper 431: Tectonic growth of a collisional continental margin: Crustal evolution of southern Alaska. *Geological Society of America Bulletin*, *431*, 95–127.

Pavlis, T. L., Sisson, V. B., Foster, H. L., Nokleberg, W. J., & Plafker, G. (1993). Mid-Cretaceous extensional tectonics of the Yukon-Tanana Terrane, trans-Alaska crustal transect (TACT), east-central Alaska. *Tectonics*, *12*(1), 103–122. https://doi.org/10.1029/92tc00860

Plafker, G. (1987). Regional geology and petroleum potential of the northern Gulf of Alaska continental margin. In D. W. Scholl, A. Grantz, & J. G. Vedder (Eds.), *Geology and resource potential of the continental margin of Western North America and adjacent ocean basins-Beaufort Sea to Baja California, Earth Sci. Ser.*, (Vol. 6, pp. 229–268). Houston, Tex: Circum-Pac. Counc. for Energy and Miner. Resour.

Plafker, G., & Berg, H. C. (1994). Overview of the geology and tectonic evolution of Alaska. In G. Plafker & H. G. Berg (Eds.), *The Geology of Alaska: Geology of North America* (Vol. G-1, pp. 989–1021). Boulder, CO: Geological Society of America.

Rioux, M., Mattinson, J., Hacker, B., Kelemen, P., Blusztajn, J., Hanghøj, K., & et al. (2010). Intermediate to felsic middle crust in the accreted Talkeetna arc, the Alaska Peninsula and Kodiak Island, Alaska: An analogue for low-velocity middle crust in modern arcs. *Tectonics*, *29*, TC3001. https://doi.org/10.1029/2009TC002541

Rossi, G., Abers, G. A., Rondenay, S., & Christensen, D. H. (2006). Unusual mantle Poisson's ratio, subduction, and crustal structure in Central Alaska. *Journal of Geophysical Research*, *111*, B09311. https://doi.org/10.1029/2005JB003956

Shapiro, N. M., Campillo, M., Stehly, L., & Ritzwoller, M. H. (2005). High-resolution surface-wave tomography from ambient seismic noise. *Science*, *307*(5715), 1615–1618. https://doi.org/10.1126/science.1108339

Sibson, R. (1980). A vector identity for the Dirichlet tessellation. *Mathematical Proceedings of the Cambridge Philosophical Society*, *87*(01), 151–155. https://doi.org/10.1017/S0305004100056589

Sibson, R. (1981). A brief description of the natural neighbor interpolant. In V. Barnett (Ed.), *Interpolating multivariate data*, (pp. 21–36). Chichester: Wiley.

Song, X., & Christensen, D. (2004). CSEDI: Observational and theoretical constraints on the structure and rotation of the inner core. International Federation of Digital Seismograph Networks. Other/Seismic Network. doi:10.7914/SN/XR_2004

Stachnik, J. C., Abers, G. A., & Christensen, D. H. (2004). Seismic attenuation and mantle wedge temperatures in the Alaska subduction zone. *Journal of Geophysical Research*, *109*, B10304. https://doi.org/10.1029/2004JB003018

Tarayoun, A., Audet, P., Mazzotti, S., & Ashoori, A. (2017). Architecture of the crust and uppermost mantle in the northern Canadian Cordillera from receiver functions. *Journal of Geophysical Research: Solid Earth*, *122*, 5268–5287. https://doi.org/10.1002/2017JB014284

Tempelman-Kluit, D. J. (1976). The Yukon crystalline Terrane: Enigma in the Canadian cordillera. *Geological Society of America Bulletin*, *87*(9), 1343–1357. https://doi.org/10.1130/0016-7606(1976)87<1343:TYCTEI>2.0.CO;2

Tian, Y., & Zhao, D. (2012). Seismic anisotropy and heterogeneity in the Alaska subduction zone. *Geophysical Journal International*, *190*(1), 629–649. https://doi.org/10.1111/j.1365-246X.2012.05512.x

Trop, J. M., & Ridgway, K. D. (2007). Mesozoic and Cenozoic tectonic growth of southern Alaska: A sedimentary basin perspective. *Geological Society of America Special Papers*, *431*, 55–94. https://doi.org/10.1130/2007.2431(04)

Turner, D. L., Forbes, R. B., Aleinikoff, J. N., McDougall, I., & Hedge, C. E., (2009). Geologic and geo-chronologic studies of the Early Proterozoic Kanektok metamorphic complex of southwestern Alaska, United States Geological Survey Open File Report, 2009-1248 (45 p).

Veenstra, E., Christensen, D. H., Abers, G. A., & Ferris, A. (2006). Crustal thickness variation in south-central Alaska. *Geology*, *34*(9), 781–784. https://doi.org/10.1130/G22615.1

Wang, Y., & Tape, C. (2014). Seismic velocity structure and anisotropy of the Alaska subduction zone based on surface wave tomography. *Journal of Geophysical Research: Solid Earth*, *119*, 8845–8865. https://doi.org/10.1002/2014JB011438

Ward, K. M. (2015). Ambient noise tomography across the southern Alaskan cordillera. *Geophysical Research Letters*, *42*, 3218–3227. https://doi.org/10.1002/2015GL063613

Ward, K. M., Zandt, G., Beck, S. L., Christensen, D. H., & McFarlin, H. (2014). Seismic imaging of the magmatic underpinnings beneath the Altiplano-Puna volcanic complex from the joint inversion of surface wave dispersion and receiver functions. *Earth and Planetary Science Letters*, *404*, 43–53. https://doi.org/10.1016/j.epsl.2014.07.022

Wessel, P., Smith, W. H. F., Scharroo, R., Luis, J. F., & Wobbe, F. (2013). Generic mapping tools: Improved version released. *Eos, Transactions American Geophysical Union*, *94*(45), 409–410. https://doi.org/10.1002/2013EO450001

Ye, S., Flueh, E. R., Klaeschen, D., & von Huene, R. (1997). Crustal structure along the EDGE transect beneath the Kodiak Shelf off Alaska derived from OBH seismic refraction data. *Geophysical Journal International*, *130*(2), 283–302. https://doi.org/10.1111/j.1365-246X.1997.tb05648.x

Zhu, L., & Kanamori, H. (2000). Moho depth variation in Southern California from teleseismic receiver functions. *Journal of Geophysical Research*, *105*(B2), 2969–2980. https://doi.org/10.1029/1999JB900322